We are IntechOpen, the world's leading publisher of Open Access books Built by scientists, for scientists

4,800
Open access books available

122,000
International authors and editors

135M
Downloads

Our authors are among the

154
Countries delivered to

TOP 1%
most cited scientists

12.2%
Contributors from top 500 universities

WEB OF SCIENCE™

Selection of our books indexed in the Book Citation Index in Web of Science™ Core Collection (BKCI)

Interested in publishing with us?
Contact book.department@intechopen.com

Numbers displayed above are based on latest data collected.
For more information visit www.intechopen.com

16

ESR Techniques for the Detection of Seismic Frictional Heat

Tatsuro Fukuchi
Yamaguchi University
Yoshida, Yamaguchi,
Japan

1. Introduction

The contribution of seismic frictional heat to the total earthquake energy budget is an important topic to elucidate earthquake rupture process. However, the frictional heat has been hardly estimated from fault rocks except melting-originated pseudotachylytes but calculated from seismological or frictional test data. The frictional heat calculated often gives a large component of the total energy budget although the San Andreas fault heat flow paradox suggests that the contribution of frictional heat may be rather small (Kanamori et al., 1998; Kanamori & Heaton, 2000; Lachenbruch & Sass, 1980, 1992). Thus, we had required any new technique to directly estimate frictional heat from fault rocks. Recent ESR (electron spin resonance) and magnetic studies of fault zones revealed that fault rocks may have been magnetized due to the thermal decomposition of iron-bearing paramagnetic or antiferromagentic minerals included in host rocks into ferrimagnetic ones by frictional heating (Fukuchi, 2003; Fukuchi et al., 2005, 2007; Ferré et al., 2005; Han et al., 2007). Since ferrimagnetic minerals commonly show huge ESR absorption due to their spontaneous magnetization, we can detect them as FMR (ferrimagnetic resonance) signals using the ESR technique. Detailed ESR analyses showed that the growth process of FMR signals during heating may fundamentally follow the zero-order reaction kinetics (Fukuchi, 2003; Fukuchi et al., 2005). Therefore, we can use FMR signals as an effective index of frictional heat. In this chapter, I will explain the basis and application of ESR techniques for the detection of seismic frictional heat using FMR signals. According to one-dimensional equations on frictional heating (McKenzie & Brune, 1972; Cardwell et al., 1978), the frictional heat strongly depends on the width of heat generation, which is equivalent to the thickness of the slip zone but not to the thickness of a pseudotachylyte vein. The thickness of the slip zone is considered to be commonly an order of millimeters or less (Kanamori and Heaton, 2000; Sibson, 2003). To actually estimate the frictional heat from a fault rock, we must sequentially detect FMR signals at a resolution of 1 mm or less. From this point of view, I develop the scanning ESR microscopic technique for sequential high-resolution measurements of FMR signals. I will introduce the case of the Nojima fault rocks in Japan.

2. Principles of ESR and FMR

A number of vacancies, interstitials and impurities exist in natural minerals. These point defects often trap unpaired electrons such as electrons ionized or holes formed in the

valence energy band by natural radiation. Some transition elements such as Fe or Mn originally have unpaired electrons at the *d*-orbit. Classical physically, an electron with negative charge may be considered to be a rotating sphere, so that the rotation of an electron, that is, the electron spin generates a circular current. Since the circular current causes a magnetic field around the electron due to the electromagnetic induction, every unpaired electron has the magnetic moment. Paired electrons in materials show no magnetic moment due to the neutralizing effect of the pairing electron spins on the basis of the Pauli exclusion principle. The electron spin is responsible for all sorts of magnetism. In this section, I will explain the principles of ESR and FMR.

2.1 Electron spin resonance

Electron spin resonance is a spectroscopic technique to detect unpaired electrons in materials. Fig. 1 shows the principle of ESR. In case of paramagnetic materials, when no external magnetic field exists around, the unpaired electrons, that is, the internal electron spins are distributed at random and as a whole show no magnetic moment. On the other hand, when the external magnetic field exits, the spins are arranged in parallel or anti-parallel with the magnetic field and separate into two energy levels (E_1 and E_2). This phenomenon is called the Zeeman splitting or Zeeman effect. Consequently, the paramagnetic materials as a whole show the magnetic moment. The difference in energy level ΔE ($=E_2-E_1$) caused by the Zeeman splitting is expressed by $\Delta E=g\beta H$, where g is a spectroscopic splitting factor (g-value), β is the Bohr magneton and H is the magnetic field. If microwaves are added to the materials under the Zeeman splitting, parallel spins with the lower energy E_1 absorb microwave power and shift to the higher energy level E_2, and

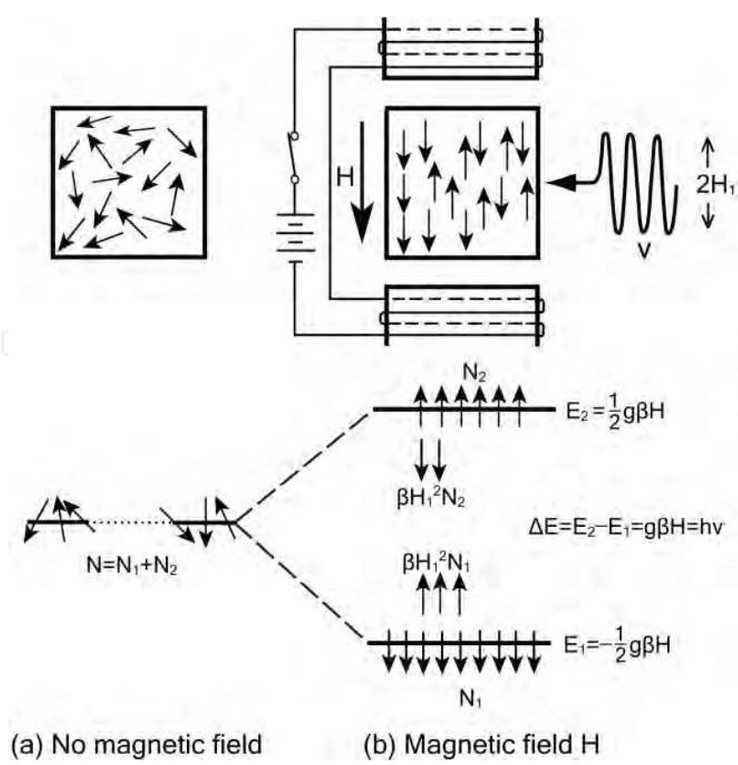

Fig. 1. Principle of electron spin resonance.

simultaneously anti-parallel spins with the higher energy E_2 emit microwaves and shift to the lower energy level E_1 when the energy $h\nu$ of microwaves are equal to the difference in energy level; $\Delta E = g\beta H = h\nu$, where h is Planck's constant and ν is the frequency of microwaves. This phenomenon is called electron spin resonance.

Since the number of the parallel spins is commonly larger than that of the anti-parallel ones, the paramagnetic materials as a whole cause the absorption of microwave power, that is, the ESR absorption. The ESR absorption is measured by sweeping the magnetic field under a fixed microwave frequency and power, and is recorded as an absorption curve using an ESR spectrometer (Fig. 2). Every paramagnetic material shows the largest absorption at the resonant magnetic field and the area of the absorption curve is proportional to the total number of the internal spins. Recent ESR spectrometers have an additional 100 kHz modulation of magnetic field to improve the S/N ratio and the rectified output is recorded as the first derivative line of the absorption curve on the recorder. We commonly call this first derivative line ESR spectrum and detect the unpaired electrons with the Zeeman energy (E_1 or E_2) as an ESR signal in the ESR spectrum (Fig. 3). Every ESR signal has an intrinsic g-value calculated from the resonant magnetic field H_r and microwave frequency ν_0 ($g=h\nu_0/\beta H_r$), so that we can identify the ESR signal by its g-value; the g-value of free electrons is 2.0023. Moreover, the linewidth and lineshape of the signal are also important physical parameters. There are two types of lineshape, the Gaussian and Lorentzian lines, in

Fig. 2. X-band ESR spectrometer

the absorption curve and the first derivative line. The relationship between the peak-to-peak linewidth ΔH_{pp} and the spin-spin relaxation time T_2 are expressed by $\Delta H_{pp} = \sqrt{\pi / 2} / (\gamma T_2)$ (Gaussian) and $\Delta H_{pp} = 1 / (\sqrt{3}\gamma T_2)$ (Lorentzian), respectively, where $\gamma = g\beta/(h/2\pi)$ (Alger, 1973). On the other hand, the peak-to-peak length of the signal is proportional to the total number of the internal spins.

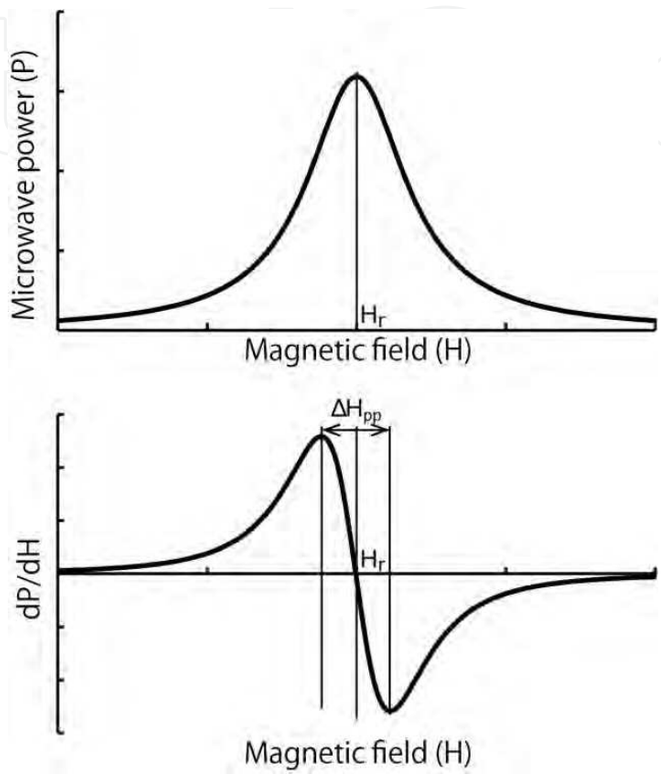

Fig. 3. ESR absorption curve and its first derivative line.

2.2 Ferrimagnetic resonance

Electron spin resonance is classified into electron paramagnetic resonance (EPR), ferromagnetic resonance, ferrimagnetic resonance, antiferromagnetic resonance (AFMR), etc. on the basis of the magnetism of the materials studied (e.g. Kittel, 2005). The principle of ferrimagnetic resonance is essentially similar to that of ferromagnetic resonance as far as the opposing magnetic moments of two sublattices in ferrimagnets precess in a magnetic field retaining their antiparallel state. In addition to this mode of precession, there is another mode that the two magnetic moments in an imperfectly antiparallel state precess on easy axes of magnetization in ferrimagnets (Kittel, 2005; Smit & Wijn, 1965). Thus, I use the term "FMR" as the abbreviation for ferrimagnetic resonance in this chapter.

In general, ferrimagnets have two sublattices consisting of different magnetic ions such as Fe^{3+} and $Fe^{3+}Fe^{2+}$ ions in magnetite. The magnetic moments of the two sublattices are opposed due to the negative exchange interaction and unequal, so that a spontaneous magnetization as a whole remains. When an external magnetic field exits, the magnetic field exerts a torque on the opposing magnetic moments and causes them to precess in one body. In case of ferromagnets, the magnetic moments are aligned in the same direction due to the

positive exchange interaction, so that the external magnetic field causes the aligned moments to precess in one body. As mentioned above, in ferrimagnetic resonance there is another mode that the two magnetic moments in an imperfectly antiparallel state precess on the easy axes of magnetization. The precession in an imperfectly antiparallel state occurs in antiferromagnets as well, where the magnetic moments of two sublattices are opposed due to the negative exchange interaction and equal, so that the precession is responsible for antiferromagnetic resonance. However, the ESR absorption due to antiferromagnetic resonance is much weaker than that due to ferrimagnetic one. On the other hand, in paramagnetic resonance, every electron's magnetic moment (electron spin) is caused to precess by the magnetic field. The frequency of precession is called the Larmor frequency. Regardless of the types of magnetism, the ESR absorption occurs when the Larmor frequency is the same as the resonant frequency, that is, the frequency of microwaves added (Kittel, 2005). In magnetic resonance, the energy $h\nu$ of electromagnetic waves with the Larmor frequency coincides with the difference in the Zeeman energy levels (Fig. 1). Since the whole of the opposing moments in ferrimagnets has much larger energy level in the magnetic field than every electron's moment, ferrimagnets show much larger ESR absorption than paramagnets. Moreover, the resonant frequency in ferrimagnetic resonance and the linewidth of the ESR absorption curve strongly depend on the orientation of the material and the magnitude of the magnetic field due to the large demagnetizing field arising from the spontaneous magnetization. The ESR signals obtained from ferrimagnets are especially called FMR (ferrimagnetic resonance) signals.

3. ESR spectra of ferrimagnetic minerals

ESR has been geologically used for investigating the characteristics of paramagnetic lattice defect centers in natural minerals or ESR dating of rock-forming minerals such as quartz or feldspars. However, there are few studies on natural ferrimagnetic minerals using ESR because magnetometers are main equipments for investigating ferrimagnetic minerals in the field of geology or geophysics. ESR spectra give us important information on the magnetism of natural minerals as well as magnetometers. The g-value of the signal is an intrinsic physical parameter calculated from the microwave frequency and resonant magnetic field, which represent the energy level of unpaired electrons in minerals. The peak-to-peak linewidth and lineshape of the signal are also important physical parameters reflecting the spin-spin relaxation time. In this section, I will show ESR spectra obtained from main ferrimagnetic minerals and explain their characteristics.

3.1 Magnetite: Fe_3O_4

Magnetite is the most famous ferrimagnetic mineral. It is a cubic crystal of the spinel group and has the inverse spinel structure, which can be expressed by$Fe^{3+}(Fe^{3+}Fe^{2+})_2O_4$, indicating that each formula unit of magnetite has one Fe^{3+} in the A sublattice and one Fe^{3+} plus one Fe^{2+} in the B sublattice. Magnetite can be produced by the oxidation of iron at high temperatures in air or steam, by heating maghemite (γ-Fe_2O_3) or hematite (α-Fe_2O_3) in a reducing atmosphere, by heating siderite ($FeCO_3$) in steam or nitrogen at dull red heat, or by heating biotite ($K(Mg,Fe^{2+})_3(Al,Fe^{3+})Si_3O_{10}(OH)_2$) in nitrogen or vacuum (Deer et al., 1992). Fig.4 shows ESR spectra obtained from powder (1–10 μm) of various magnetite samples. The samples are respectively natural magnetite (≤10μm) distributed at Hanaidani Mine in

Shimane, Japan (Nichika Corporation, MJ09) (a), synthetic magnetite (~1μm) with high purity (WAKO Pure Chemical Industries, JW090103) (b), magnetite produced from natural biotite (≤10μm) distributed in the Uchinoura granite in southern Kyushu, Japan by heating at 1000°C for 1 h under 0.5 Pa (c), and magnetite produced from natural siderite (≤10μm) distributed in Guelmin Es-Semara Region, Morocco (Hori Mineralogy Ltd.) by heating at 500°C for 5 min. under 0.6 Pa (d). The spectrum c) is magnified to 50×. Measurement conditions are as follows and the same conditions are used for the other spectra in this chapter: microwave frequency; 9.43 GHz, microwave power; 1 mW, modulation width; 100 kHz 0.05 mT, sweep speed; 8 min/sweep, accumulation; 3 times, measurement temperature; room temperature. The g-value calculated from the spectra is 2.70−7.15 and the peak-to-peak linewidth of the FMR signals is 219−358 mT. The g-value tends to shift toward the lower magnetic field with increasing grain size due to the demagnetizing field. Siderite is a brownish trigonal mineral in the calcite group, while biotite is a black monoclinic mineral in the mica group. Since siderite and biotite are paramagnetic, both originally show paramagnetic signals, that is, EPR signals.

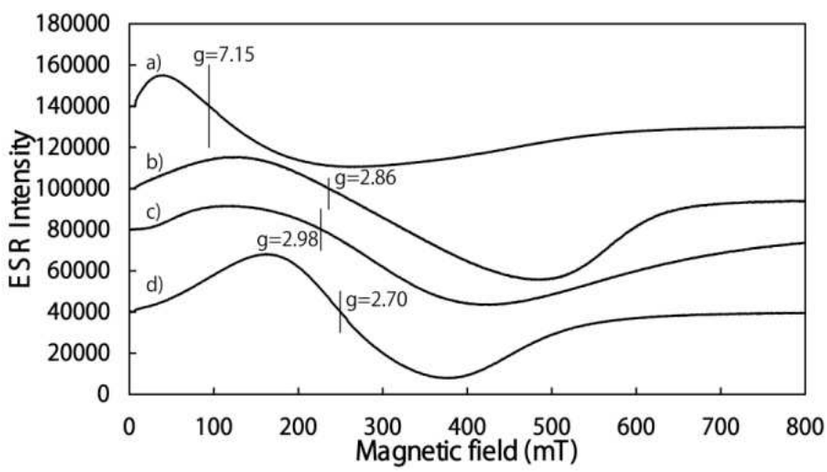

Fig. 4. ESR spectra obtained from various magnetite samples.

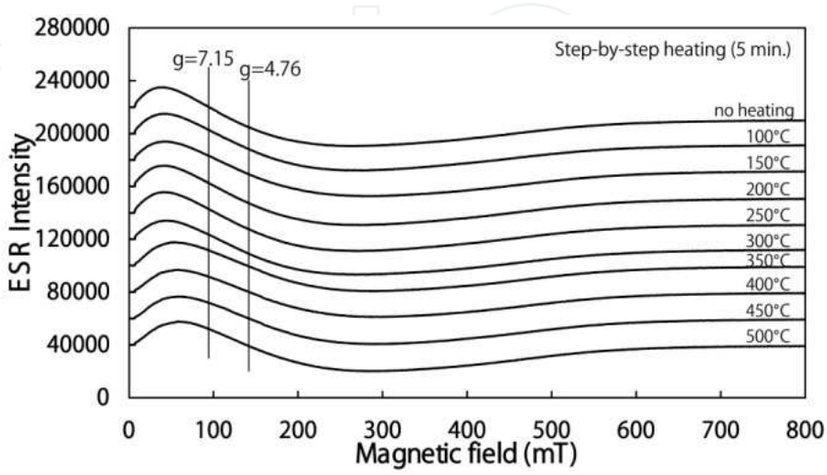

Fig. 5. Variation of the ESR spectrum of natural magnetite with step-by-step heating in air.

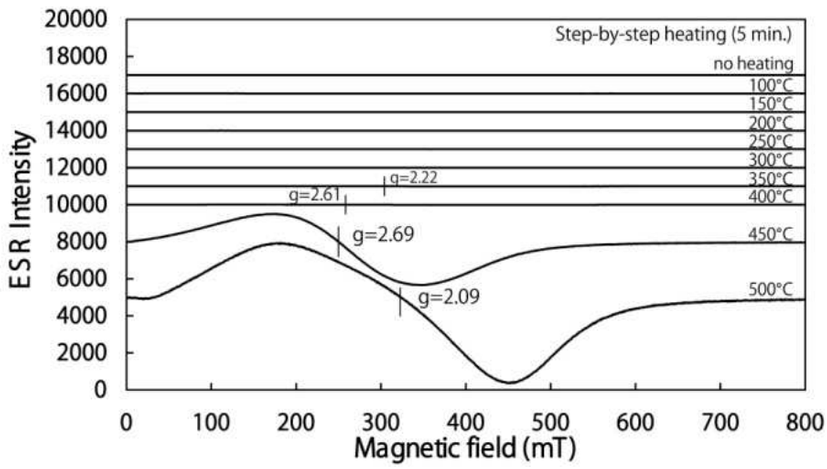

Fig. 6. Variation of the ESR spectrum obtained from natural siderite with step-by-step heating in air.

Fig. 5 shows the result from step-by-step heating experiments at 100–500°C in air. The heating duration is 5 minutes for each temperature. The natural magnetite same as the spectrum a) in Fig. 4 was used for the heating experiments. Magnetite is usually oxidized and changed into maghemite or hematite by heating in air, and the g-value of the FMR signal obtained from the natural magnetite shifts from 7.15 to 4.76 with heating. Although the signal peak becomes broader with the oxidation due to heating, its lineshape does not change so much; the peak-to-peak linewidth is in the range of 220−239 mT. This means that the oxidation may be limited to only the surface of the magnetite particles. On the other hand, Fig.6 shows ESR spectra obtained from natural siderite by step-by-step (5 min.) heating in air. The natural siderite same as the spectrum d) in Fig. 4 was used for the heating experiments. The FMR signal of magnetite produced from siderite by heating strikingly increases at 450°C, and then its lineshape is distorted at 500°C due to the production of maghemite or hematite. The FMR signal detected at 450°C in air has almost the same g-value, peak-to-peak linewidth and lineshape as that of magnetite detected at 500°C in vacuum (Fig. 4d). However, the g-value somewhat shifts from 2.69 to 2.09 with heating, while the peak-to-peak llinewidth extremely changes from 170 to 272 mT. Since the magnetite produced by thermal decomposition of siderite may consist of extremely fine crystals or amorphous particles, it is easily oxidized under an oxidizing environment.

3.2 Maghemite: γ-Fe_2O_3

Maghemite is a popular ferrimagnetic mineral and widely used as a material for magnetic recorders. It is a cubic crystal of the spinel group and has the spinel structure expressed by $Fe^{3+}(Fe^{3+}Fe^{3+}{}_{2/3},V_{1/3})O_4$ where V is a vacancy, indicating that magnetite is oxidized to maghemite by changing the valence state of two thirds of the original Fe^{2+} to Fe^{3+} while simultaneously removing one third of the original Fe^{2+} from the B sublattice. This removal occurs by diffusion producing vacancies in the spinel structure where a Fe^{2+} cation had previously resided; these vacancies account for the name cation-deficient spinel. Since ferrimagnetism of magnetite results from Fe^{2+} in the B sublattice, the removal of one third of these cations decreases saturation magnetization from 480 G (4.8×10^5 A/m) for magnetite to 420 G (4.2×10^5 A/m) for maghemite (Butler, 1992). Pure maghemite is commonly metastable

and irreversibly changes its crystal structure into a hexagonal one, that is, α-Fe_2O_3 (hematite) on heating to 300–500°C. However, the transformation temperature of natural maghemite into hematite is often over 500–700°C because maghemite is stabilized with impurities inside the crystal (e.g. Fukuchi et al., 2007). As for the formation of natural maghemite, besides the oxidation of magnetite, the following three processes are pointed out on the basis of the studies of ferrimagnetic minerals in soils (Butler, 1992):

1. The formation of maghemite from iron oxides or oxyhydroxides by repeated oxidation-reduction cycles during soil formation.
2. The conversion of paramagnetic iron-bearing minerals by natural burning (above ~200 °C) in the presence of organic matter.
3. The dehydration of lepidocrocite (γ-FeOOH).

Fig. 7 shows the ESR spectrum obtained from powder (≤1μm) of synthetic maghemite and its variation with step-by-step heating (5 min.) in air. The synthetic maghemite (≤1μm) with high purity (Kojundo Chemical Lab, FE006PB) was used for the heating experiments. Maghemite shows a quite different lineshape from magnetite. The signal peak around the lower magnetic field (~100 mT) obtained from maghemite is much sharper than that from magnetite (Fig.4). The g-value calculated from the spectra is in the range of 3.26−3.34 and the peak-to-peak linewidth of the FMR signals is 346−358 mT. The FMR signal of maghemite hardly changes its lineshape during heating until 500°C and thermally shows high stability although pure maghemite transforms into hematite by heating to 300–500°C.

On the other hand, Fig. 8 shows ESR spectra obtained from natural and synthetic hematites with those from synthetic lepidocrocite and goethite (α-FeOOH) and natural limonite ($FeOOH(nH_2O)$). The samples are synthetic hematite (≤10 μm) with high purity (WAKO Pure Chemical Industries, JW090282) (a), natural hematite (specularite, ≤10 μm) distributed in Antananarivo, Madagascar (Hori Mineralogy Ltd.) (b), synthetic goethite (~1μm) with high purity (Kojundo Chemical Lab, FEI16PB) (c), synthetic lepidocrocite with high purity (≤10 μm, Kojundo Chemical Lab, FEI17PB) (d), and natural limonite (≤10 μm) distributed in Hwanghae-do, North Korea (Nichika Corporation, MU262) (e). Small signals like spines detected between 300 and 400 mT in the spectrum b) are Mn^{2+} markers. Hematite is a trigonal mineral of the corundum structure and shows parasitic ferromagnetism, which is a

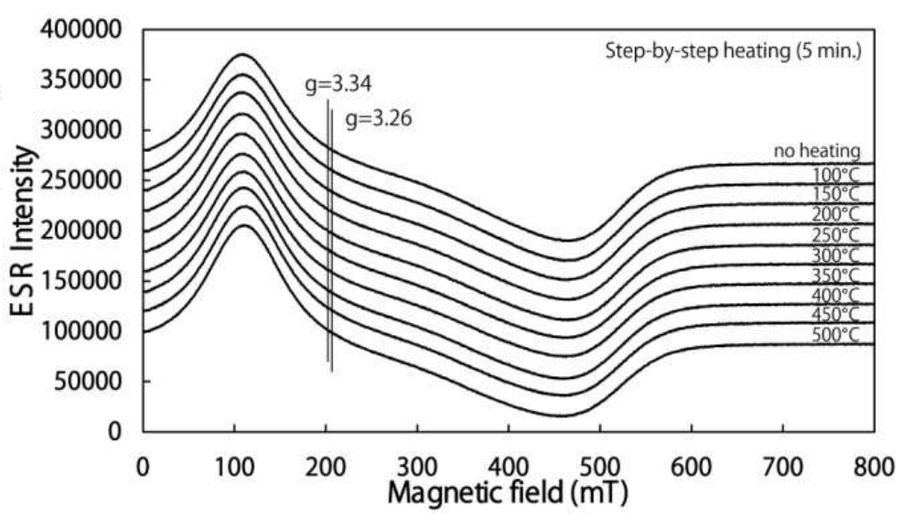

Fig. 7. Variation of the ESR spectrum of synthetic maghemite with step-by-step heating in air.

kind of antiferromagnetism. Hematite has an asymmetrical antiferromagnetic structure, so that it shows a weak spontaneous magnetization and ESR absorption (Fig. 8a). On the other hand, natural hematite (specularite) shows a quite different ESR signal from the synthetic hematite. It has the g-value of 10.8, which is much larger than that of 2.35 obtained from the synthetic hematite.

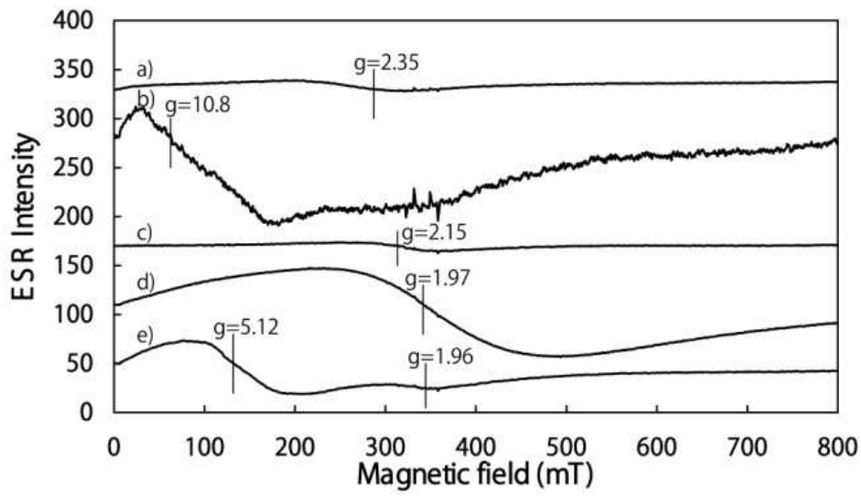

Fig. 8. ESR spectra obtained from powder of hematite, goethite, lepidocrocite and limonite.

Lepidocrocite is a monoclinic (or trigonal) paramagnetic crystal at room temperature, however shows antiferromagnetism at the Néel temperature of 77K. Therefore, lepidocrocite shows a paramagnetic signal at room temperature (Fig. 8d). A strong FMR signal of maghemite comes to be detected from heated lepidocrocite due to thermal dehydration; $2\gamma\text{-FeOOH} \rightarrow \gamma\text{-Fe}_2\text{O}_3 + \text{H}_2\text{O}$. Fig. 9 shows the variation of the ESR spectrum of lepidocrocite with step-by-step heating (5 min.) in air. The synthetic lepidocrocite same as the spectrum d) in Fig. 8 was used for the heating experiments. The FMR signal of maghemite produced from pure lepidocrocite by heating strikingly increases at 300°C. This suggests that the maghemite produced from lepidocrocite changes from a superparamagnet to a ferrimagnet between 250 and 300°C. The g-value is 2.26–2.31 and the peak-to-peak linewidth is 166–192 mT. The lineshapes of the FMR signals detected are different from those of maghemite with high crystallinity (Fig. 7). Moreover, Fig. 10 shows the result from isothermal annealing experiments at 250°C using the synthetic lepidocrocite. The lineshape and g-value of the signal obtained from the lepidocrocite characteristically change with heating time. The g-value shifts from 2.0 to 2.18 since the demagnetizing field causes the resonant magnetic field to shift toward the lower field (Fukuchi et al., 2007). The peak-to-peak linewidth also changes from 24 to 174 mT with heating time. In general, the maghemite produced from lepidocrocite has low crystallinity and shows an FMR signal with much lower g-value and peak-to-peak linewidth than maghemite with high crystallinity or one produced by the oxidation of magnetite (Figs. 5–7). Strictly speaking, such an FMR signal may be called superparamagnetic signal although it is difficult to distinguish between the superparamagnetic and ferrimagnetic signals. In this chapter, I use the term FMR signal for ESR signals derived from both superparamagnetic and ferrimagnetic maghemites. As mentioned later, the FMR signals detected from the Nojima fault rocks in Japan show almost the same characteristics as the superparamagnetic signal detected from the heated lepidocrocite.

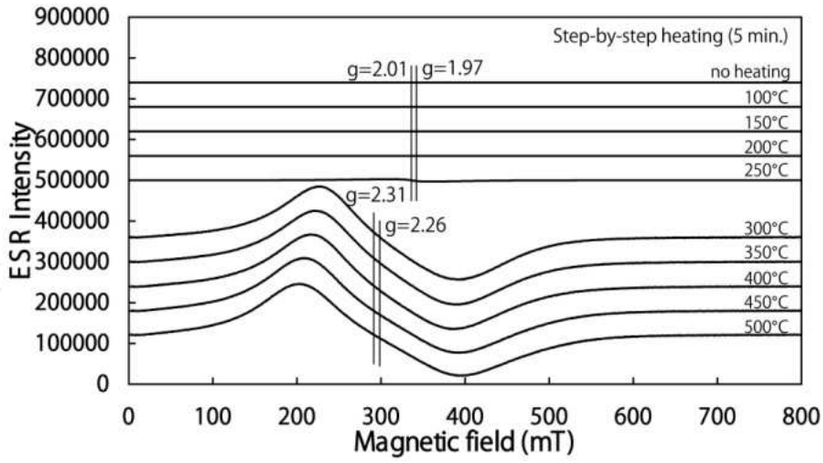

Fig. 9. Variation of the ESR spectrum of lepidocrocite with step-by-step heating in air.

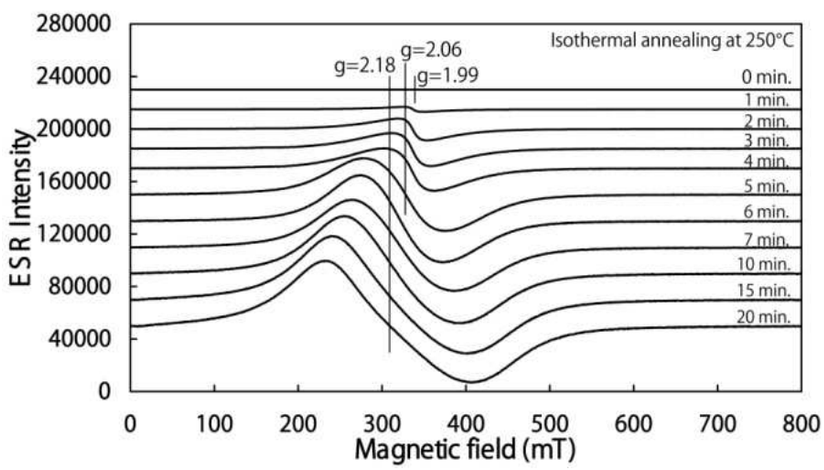

Fig. 10. Variation of the ESR spectrum of lepidocrocite with isothermal annealing at 250°C in air.

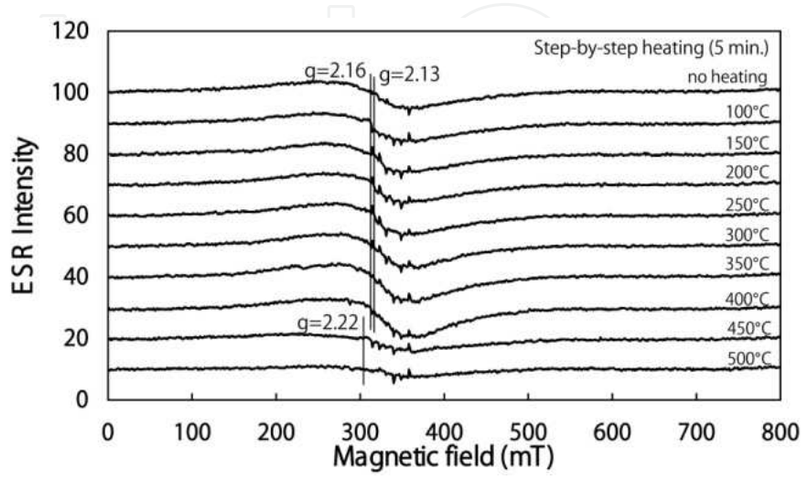

Fig. 11. Variation of the ESR spectrum of goethite with step-by-step heating in air.

Goethite is an orthorhombic mineral and a polymorph of lepidocrocite. It changes into hematite due to thermal dehydration by heating at 300–400°C; $2\alpha\text{-FeOOH} \rightarrow \alpha\text{-Fe}_2\text{O}_3 + \text{H}_2\text{O}$. Fig. 11 shows the variation of the ESR spectrum of goethite with step-by-step heating (5 min.) in air using the synthetic goethite (Fig. 8c).
Goethite is an antiferromagnet however exhibits a weak ferromagnetism as well as hematite. The signal detected once increases with producing hematite, and then decays above 400°C. The g-value is in the range of 2.13–2.22 and the peak-to-peak linewidth is 92–136 mT. The characteristics of the signal are very similar to those obtained from the heated lepidocrocite although the signal intensity is very weak. On the other hand, limonite consists of cryptocrystalline goethite and lepidocrocite along with absorbed water or some hematite, so that it has a complex ESR spectrum derived from these minerals (Fig. 8e).

3.3 Pyrrhotite: $Fe_{1-x}S$ ($0 \leq x < 0.125$)

Pyrrhotite has the approximate composition of FeS but always contains less iron than is indicated by this formula. Hence, it is expressed by the generic formula of $Fe_{1-x}S$, where $0 \leq x < 0.125$. Pyrrhotite is a monoclinic or hexagonal crystal of the nickel arsenide (NiAs) structure and consists of several superstructures due to the presence and ordering of vacancies within the structure. In pyrrhotite, two antiparallel coupled sublattices containing iron cations exist and the number of iron cations in the opposing sublattices are unequal, so that it is responsible for the ferrimagnetism of pyrrhotite. Troillite (FeS) is antifferomagnetic and occurs mainly in meteories and lunar rocks. Pyrrhotite can be produced by the direct combination of iron and sulphur and by heating pyrite (FeS_2) in an atmosphere of H_2S at 550°C. In the Fe-S system, the pyrrhotite in equilibrium with pyrite above 400°C shows increasing iron deficit with increasing temperature (Deer et al., 1992). Fig. 12 shows ESR spectra obtained from natural pyrrhotite, synthetic troillite and synthetic pyrite. The samples used are natural pyrrhotite (≤10μm) distributed at Yanahara Mine in Okayama, Japan (Nichika Corporation, MU123) (a), synthetic troillite (≤10 μm) with high purity (Kojundo Chemical Lab, FEI06PB) (b), and synthetic pyrite (≤10 μm) with high purity (Kojundo Chemical Lab, FEI07PB) (c). The natural pyrrhotite shows very weak and broad ESR absorption, while the troillite has a similar ESR spectrum to natural hematite, that is,

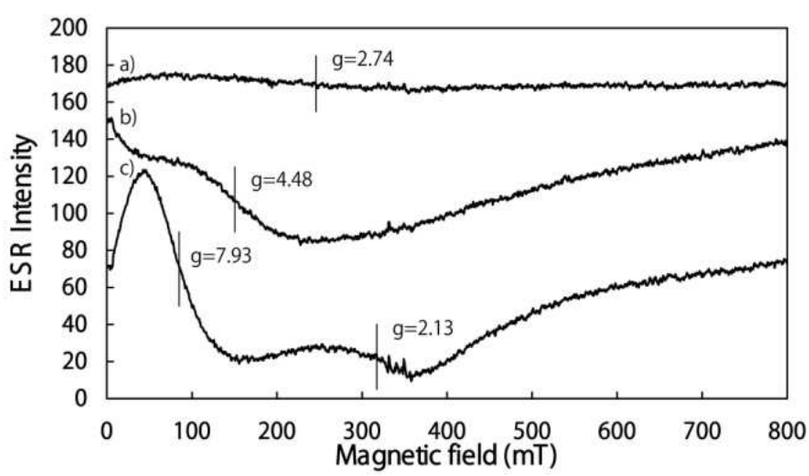

Fig. 12. ESR spectra obtained from powder of natural pyrrhotite, and synthetic troillite and pyrite.

specularite (Fig. 8b). On the other hand, pyrite is a cubic mineral and shows paramagnetism. The synthetic pyrite shows an intermediate spectrum of specularite and troillite.

4. ESR spectra of fault rocks

In general, ESR spectra obtained from natural minerals present various phases, because they reflect multiple geological events having taken place during the long geological time. Especially, faults repeatedly move, so that the fault rocks have been influenced by multiple frictional heating events and show complicated ESR spectra consisting of overlapping multiple signals. Therefore, we must separate individual signals from the whole spectrum on the basis of the physical parameters such as the g-value or peak-to-peak linewidth. In this section, I will introduce some examples of magnetized fault rocks and attempt to identify the FMR signals detected from the fault rocks by comparing their physical parameters with those obtained from known ferrimagnetic minerals.

4.1 Nojima fault

The Nojima fault is one of the most famous earthquake faults in Japan, which caused the 1995 Kobe earthquake (Magnitude 7.3). After the Kobe earthquake, the black fault rock with high magnetic susceptibility was found in the Nojima fault zone (Otsuki et al., 2003; Fukuchi, 2003). This fault rock consists of multiple sheets of a few mm wide veins, each of which was produced from granitic fault gouge during ancient earthquakes (Fig. 13). Despite no obvious melting textures, it was named "Nojima pseudotachylyte" as a descriptive name that comes from its glassy dark appearance and intrusive structure. Fig. 14 shows the ESR spectra obtained from the pseudotachylyte veins (PT-1 and PT-2) and baked fault gouge (GG-1) with the original fault gouge (NG-1) that is the source rock of the pseudotachylyte veins. Besides a

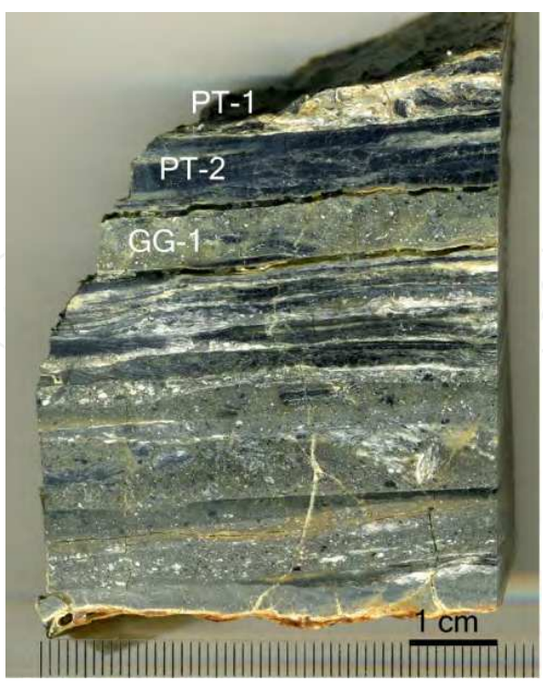

Fig. 13. Nojima pseudotachylyte veins in the Nojima fault zone.

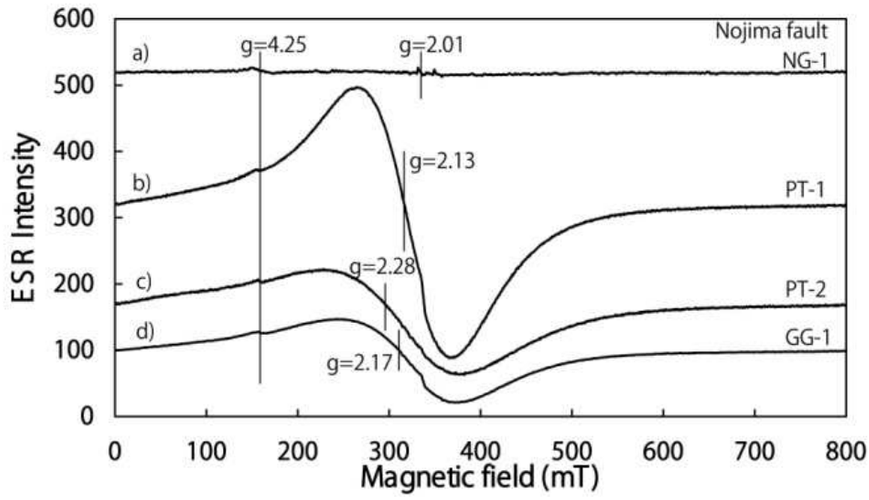

Fig. 14. ESR spectra obtained from the Nojima pseudotachylyte veins and fault gouge.

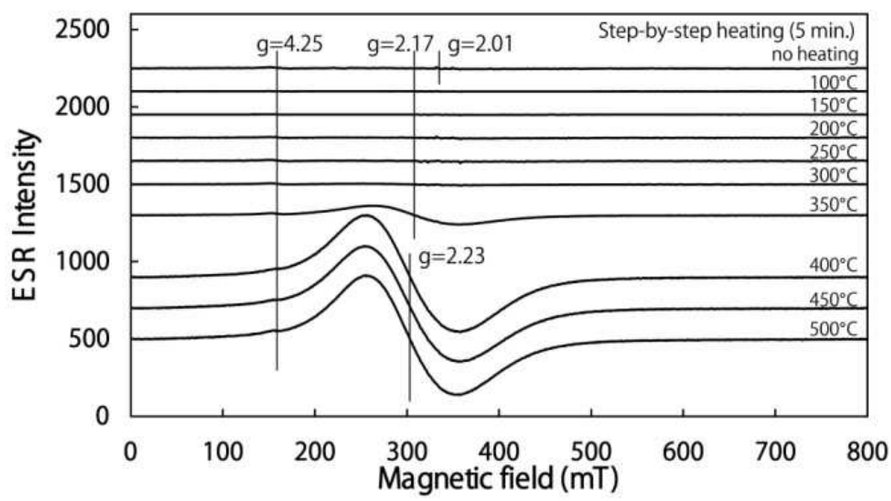

Fig. 15. Variation of the ESR spectrum obtained from the Nojima fault gouge with step-by-step heating in air.

paramagnetic Fe^{3+} ion signal at g=4.25 and other paramagnetic signals derived from quartz or clay minerals between 300–400 mT, no FMR signal is detected from the original fault gouge (NG-1). This means that there originally existed no ferrimagnetic mineral inside the fault gouge, because the FMR signals derived from magnetite and maghemite are thermally so stable, as shown in Figs. 5–7, that they cannot perfectly disappear by later frictional heating or the oxidation caused by the heating. The g-values and peak-to-peak linewidths of the signals detected from the black veins and baked gouge are 2.13–2.28 and 102–155 mT, respectively. Hence, these signals have almost the same physical parameters as the superparamagnetic signals detected from heated lepidocrocite rather than maghemite with high crystallinity or one produced by the oxidation of magnetite (Figs. 6, 7, 9 and 10).

Moreover, Fig. 15 shows the variation of the ESR spectrum obtained from the original fault gouge (NG-1) by step-by-step heating (5 min.) in air (Fig. 14a). The g-value and peak-to-

peak linewidth of the signals detected by heating are 2.17–2.23 and 102–128 mT, so that they are consistent with those detected from the Nojima fault rocks and from the superparamagnetic signals of baked lepidocrocite. This strongly suggests that the magnetic source of the Nojima pseudotachylyte and baked gouge may be superparamagnetic maghemite produced by thermal dehydration of lepidocrocite, and besides that the Nojima pseudotachylyte may have been produced in an oxidizing environment.

4.2 Uchinoura shear zone

The Uchinoura shear zone is distributed in the Middle Miocene Osumi granodiorite pluton, which is located at the southern end of the Kyushu Island in Japan about 170 km away from the Nankai Trough subduction zone, and consists of a series of ENE trending faults (Fabbri et al., 2000). Along the Uchinoura shear zone, pseudotachylyte veins are exposed with cataclastic rocks such as foliated cataclasite. Fig. 16 shows a photograph of the black pseudotachylyte vein (PT) intruded into foliated cataclasite (FC). ESR spectra obtained from the Osumi granodiorite (OG), foliated calaclasite (FC) and pseudotachylyte vein (PT) are shown in Fig. 17. The Osumi granodiorite has a paramagnetic Fe^{3+} ion signal at g=4.23 and another paramagnetic signal between 300–400 mT similar to the signal of goethite and/or hematite (Fig. 8). On the other hand, the foliated cataclasite and pseudotachylyte vein have an FMR signal with the g-value of 2.57–2.88 and the peak-to-peak linewidth of 218–223 mT. These physical parameters obtained from the fault rocks are consistent with those from magnetite, and indeed we can detect similar FMR signals by heating biotite in the Osumi granodiorite over 800–1000°C in vacuum (Fig. 4c). For producing magnetite from biotite by heating in vacuum, high temperatures over 600–800°C are necessary, while biotite can be easily oxidized by heating in air and changes into hematite without producing magnetite. The ESR data indicate that the pseudotachylyte veins along the Uchinoura shear zone may have been formed by frictional heating in a reducing environment at depths.

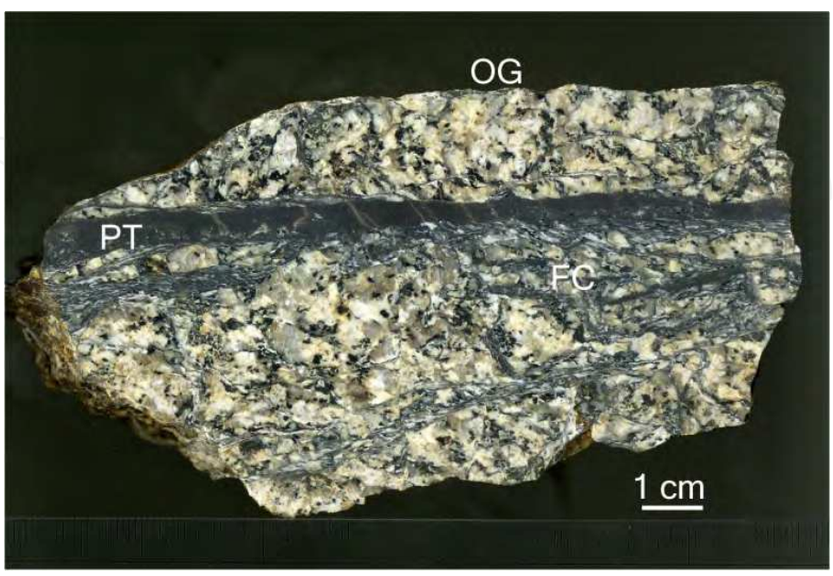

Fig. 16. Pseudotachylyte veins distributed along the Uchinoura shear zone.

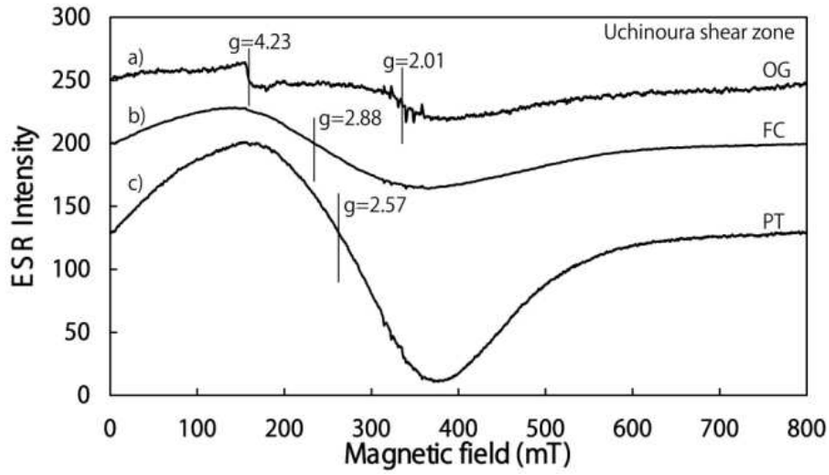

Fig. 17. ESR spectra obtained from the Osumi granite, foliated cataclasite and pseudotachylyte veins distributed along the Uchinoura shear zone.

4.3 Taiwan Chelungpu fault

The Taiwan Chelungpu fault moved in the 1999 Chi-Chi earthquake (Magnitude 7.6), which occurred in the collision zone of the Eurasian and Philippine Sea plates. After the earthquake, the Taiwan Chelungpu Fault Drilling Project (TCDP) was launched in 2002 to elucidate the rupture process caused in a subduction seismogenic zone, and continuous drill cores were collected from two main boreholes (Holes A and B) penetrating through the Chelungpu fault plane at depths (Ma et al, 2006). In the Hole B cores, there are three major fault zones at about 1136 m, 1194 m and 1243 m depths, in which a black material zone respectively exists. The black material zone is considered to have been formed by frictional heating (Hirono et al., 2006). Fig. 18 shows the black material zone in the 1194 m major fault zone. Black fault gouge exists along with the black indurated material, which may have been produced by frictional melting. Fig. 19 shows ESR spectra obtained from the black and gray gouges and black indurated material. Besides a paramagnetic Fe^{3+} ion signal (g=4.23) and an organic radical (g=2.004) (Fukuchi et al., 2007), a broad signal (g=2.27–2.44 and

Fig. 18. Black material zone distributed at about 1194 m depth in the TCDP Hole B cores.

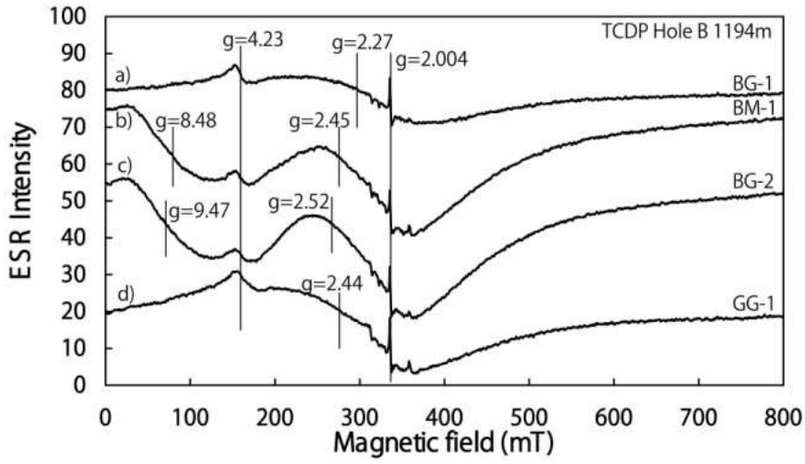

Fig. 19. ESR spectra obtained from the black material zone Taiwan Chelungpu fault zone.

ΔH_{pp}=150–173 mT) is detected from one black gouge and the gray gouge (BG1 and GG-1), while two types of large signal (g=8.48–9.47 and g=2.45–2.52) are detected from the black indurated material (BM-1) and another black gouge (BG-2). The broad signal at g=2.27–2.44 may be identified with the FMR signal of maghemite produced from lepidocrocite and/or hematite, while the lineshape of the large signal at g=8.48–9.47 is similar to that of the signal with g=10.8 obtained from specularite (Figs. 8 and 9). On the other hand, the signal at g=2.45–2.52 has the peak-to-peak linewidth of 114–123 mT, so that it may be derived from maghemite produced from lepidocrocite, goethite or hematite produced from goethite (Figs. 10 and 11). These results suggest that the black material zone may have been repeatedly subjected to frictional heating in an oxidizing environment.

5. Basic equations for frictional heat analysis

Coseismic frictional heat can be detected by measuring FMR signals in fault rocks. To calculate the frictional heat from FMR signals, we need the chemical kinetics for FMR signals besides the diffusion equations of frictional heat. As mentioned above, there are mainly two FMR signals derived from maghemite and magnetite among the FMR signals detected from natural fault rocks. Although the two FMR signals have different g-values, peak-to-peak linewidths and lineshapes, the growth processes of these signals are essentially based on the same mechanism, that is, the thermal decomposition and grain growth during heating, and are fundamentally expressed by the zero-order kinetic equation (Fukuchi, 2003). Actual fault rocks may have a mixed signal of the two FMR signals with other paramagnetic or antiferromagnetic signals, so that we must experimentally investigate the chemical kinetics on every fault rock. In this section, I will explain the basic equations necessary for calculating the frictional heat from FMR signals by inversion.

5.1 Chemical kinetics of ESR signals

There are a lot of studies on the chemical kinetics of ESR signals detected from paramagnetic minerals in connection with luminescence emitted from them. ESR signals derived from electrons or holes trapped at lattice defects in paramagnetic minerals commonly decay with

time on heating and their decay processes may be expressed by the 1st, 2nd order or other kinetic model (Fukuchi, 1989, 1992; Fukuchi & Imai, 2001; Ikeya, 1993). On the other hand, the chemical kinetics of FMR signals has been studied using the FMR signal of maghemite in the Nojima fault gouge (Fukuchi, 2003; Fukuchi et al., 2005). The FMR signal of maghemite grows with the thermal decomposition of lepidocrocite and the grain growth of maghemite during heating. As shown in Fig. 10, the signal intensity increases with time on heating and its growth process follows the zero-order reaction kinetics; $dI/dt=a$, where I is the FMR signal intensity, t is time and a is the velocity constant. a is equivalent to the slope of the growth line of the FMR signal; $I=at$. When the temperature T is constant, a is expressed by the Arrhenius' equation; $a=\nu\exp[-E/RT]$, where ν is the frequency factor, E is apparent activation energy and R is the gas constant. Now we consider one-dimensional thermal conduction. When the temperature changes with distance x and time t, the velocity constant $a(x,t)$ is expressed by

$$a(x,t) = \nu \exp\left[-\frac{E}{RT(x,t)}\right] \tag{1}$$

where $T(x,t)$ is the temperature at distance x and time t. When we deal with seismic frictional heating, $T(x,t)$ means the frictional heat temperature at a distance from a fault plane (x=0) and a passing time t after earthquake rupture. If we set the FMR signal intensity as $I(x,t)$, $\partial I(x,t)/\partial t=a(x,t)$. Then, $I(x,t)$ is expressed by

$$I(x,t) = \int_0^t a(x,t)dt = \int_0^t \nu \exp\left[-\frac{E}{RT(x,t)}\right]dt \tag{2}$$

ν and E are experimentally determined from the Arrhenius plot of velocity constants measured at various temperatures (Fukuchi, 2003). In actual frictional heat analysis, we must collect the fault rock sample with a finite thickness. Therefore, when the sampling thickness is w_0, the mean FMR signal intensity F (w_0, x, t) between the distances of x and $x+w_0$ from the fault plane is expressed as follows (Fukuchi et al., 2005):

$$F(w_0,x,t) = \frac{1}{w_0}\int_x^{x+w_0} I(x,t)dx = \frac{1}{w_0}\int_x^{x+w_0}\int_0^t a(x,t)dtdx = \frac{1}{w_0}\int_x^{x+w_0}\int_0^t \nu \exp\left[-\frac{E}{RT(x,t)}\right]dtdx \tag{3}$$

5.2 One-dimensional diffusion models of frictional heat

As for the temperature during seismic frictional heating, some one-dimensional diffusion models of frictional heat have been proposed (e.g. McKenzie & Brune, 1972; Cardwell et al., 1978). According to McKenzie & Brune (1972), the equation for the diffusion of frictional heat is expressed by

$$\rho C_p \frac{\partial T}{\partial t} = k^* \frac{\partial^2 T}{\partial x^2} + Q(x,t) \tag{4}$$

where ρ is the density, C_p is the specific heat, k^* is the thermal conductivity, and Q is the frictional heat generation per unit volume and time. When we assume that $T=T_0$ and Q=0 for t<0, the solution of eq.4 can be written down as follows:

$$T(x,t) = T_0 + \frac{1}{2\rho C_p \sqrt{\pi K}} \int_0^t \int_{-\infty}^{\infty} \exp\left[-\frac{(x-x_0)^2}{4K(t-t_0)} \right] \frac{Q(x_0,t_0)}{\sqrt{t-t_0}} dx_0 dt_0 \tag{5}$$

where K is the thermal diffusivity ($K=k^*/\rho C_p$). When we further assume that the frictional heat generation is restricted to a fault plane, Q is expressed by

$$\left.\begin{aligned} Q(x_0,t_0) &= 0 \qquad (t_0 < 0, t_0 > t_1) \\ &= \delta(x_0)\frac{\sigma_f D}{t_1} \qquad (0 \le t_0 \le t_1) \end{aligned}\right\} \tag{6}$$

where $\delta(x_0)$ is the Dirac delta function, σ_f is the frictional shear stress, D is the displacement, and t_1 is the slip duration (McKenzie & Brune, 1972). Then, eq.5 is expressed as follows:

$$\begin{aligned} T(x,t) &= T_0 + \frac{\sigma_f D}{\rho C_p t_1} \left\{ \sqrt{\frac{t}{\pi K}} exp\left[-\frac{x^2}{4Kt} \right] - \frac{x}{2K} erfc\left[-\frac{x}{2\sqrt{Kt}} \right] \right\}, \qquad 0 \le t \le t_1 \\ &= T_0 + \frac{\sigma_f D}{\rho C_p t_1} \left[\left\{ \sqrt{\frac{t}{\pi K}} exp\left[-\frac{x^2}{4Kt} \right] - \sqrt{\frac{t-t_1}{\pi K}} exp\left[-\frac{x^2}{4K(t-t_1)} \right] \right\} \right. \\ &\quad \left. -\frac{x}{2K} \left\{ erfc\left[-\frac{x}{2\sqrt{Kt}} \right] - erfc\left[-\frac{x}{2\sqrt{K(t-t_1)}} \right] \right\} \right], \qquad t > t_1 \end{aligned} \tag{7}$$

On the other hand, when we assume that the frictional heat is generated with a finite thickness, Q is expressed by

$$\left.\begin{aligned} Q(x_0,t_0) &= 0 \qquad (t_0 < 0, t_0 > t_1) \\ &= \frac{\sigma_f D}{w t_1} \left[H\left(x_0 + \frac{w}{2} \right) - H\left(x_0 - \frac{w}{2} \right) \right] \qquad (0 \le t_0 \le t_1) \end{aligned}\right\} \tag{8}$$

where w is the width of heat generation and H is the Heavyside step function (Cardwell et al., 1978). Then, eq.5 is expressed as follows:

$$\begin{aligned} T(x,t) &= T_0 + \frac{\sigma_f D}{2\rho C_p w t_1} \int_0^t \left\{ erf\left[\frac{x+(w/2)}{\sqrt{4K(t-t_0)}} \right] - erf\left[\frac{x-(w/2)}{\sqrt{4K(t-t_0)}} \right] \right\} dt_0, \qquad 0 \le t \le t_1 \\ &= T_0 + \frac{\sigma_f D}{2\rho C_p w t_1} \int_0^{t_1} \left\{ erf\left[\frac{x+(w/2)}{\sqrt{4K(t-t_0)}} \right] - erf\left[\frac{x-(w/2)}{\sqrt{4K(t-t_0)}} \right] \right\} dt_0, \qquad t > t_1 \end{aligned} \tag{9}$$

Since the frictional heat temperature calculated from eq.9 begins to diverge to infinity when w<0.5 mm (Fukuchi et al., 2005), then we should use eq.7 in place of eq.9.

The maximum temperature rise ΔT at $t=t_1$ and $x=0$ obtained from eq.7 is expressed as follows (McKenzie & Brune, 1972):

$$\Delta T = T_m - T_0 = \frac{\sigma_f D}{\rho C_p \sqrt{\pi K t_1}} \tag{10}$$

where T_m is the maximum temperature. Eq.10 is valid when $w \approx 0$. On the other hand, when $w \geq 0.5$ mm, the maximum temperature rise ΔT at $t=t_1$ and $x=0$ obtained from eq.9 is expressed by

$$\Delta T = T_m - T_0 = \frac{\sigma_f D}{\rho C_p w} \tag{11}$$

5.3 Frictional heat energy

The product of the frictional shear stress and displacement, that is, $\sigma_f D$ in eqs.6−11 is equivalent to the frictional heat energy per unit area φ_H. In case of large earthquakes, frictional heat is most probably generated with a finite thickness of slip zone; $w \gg 0$. Then, the relationship between φ_H and w for a fault can be expressed by Eq.11 and φ_H is proportional to w (Fig.20). When we regard T_m as a melting point, φ_H means the frictional melting energy per unit area φ_M. Therefore eq.11 can give constraints on the relationship between φ_M and w. Once frictional melting occurs in a shear zone, the temperature of melt is maintained at a melting point until the materials in the shear zone are completely molten because the subsequent frictional heat should be consumed as latent heat. In addition, once frictional melting occurs, the friction coefficient immediately drops towards zero (Di Toro et al., 2004). Thus, T_m should not be beyond the melting point and besides φ_H should not be beyond φ_M. On the other hand, φ_H increases with increasing the depth of the fault because σ_f is proportional to the normal stress σ_n when the coefficient of friction is constant over the fault plane. This means that φ_H per unit depth, that is, the frictional heat energy per unit volume ψ_H is more meaningful than φ_H. When ψ_H is constant over the fault plane, the mean value $\bar{\varphi}_H$ of φ_H for a fault is expressed using the focal depth z_0 as follows:

$$\bar{\varphi}_H = \frac{1}{z_0}\int_0^{z_0} \psi_H z dz = \frac{\psi_H z_0}{2} \tag{12}$$

Fukuchi et al. (2005) estimated the frictional heat energy for the Nojima fault using the FMR signal detected from the fault gouge in the Nojima fault 500m drill cores. The φ_H value of the

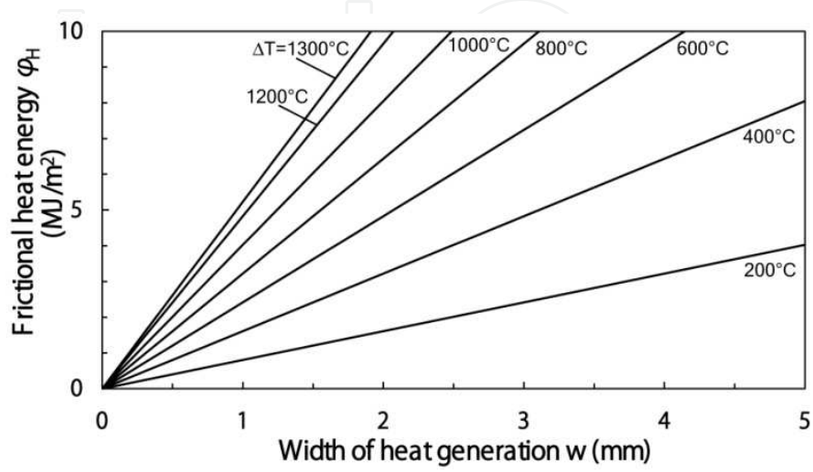

Fig. 20. Relationship between frictional heat energy and the width of heat generation.

Nojima fault at about 390 m in depth was calculated at 20.61 MJ/m^2 with the w value of 14 mm by inversion using eqs.3 and 7 or 9. However, the Nojima fault has moved frequently during the Quaternary period, so that the value obtained means the total frictional heat energy since the formation of the fault gouge. According to the geological analysis of the 500 drill cores, the total uplift along the fault plane at about 390m in depth was estimated at about 230 m (Murata et al. 2001). Therefore, the φ_H value per unit faulting may be calculated at about 0.18 MJ/m^2 when the displacement is 2.0 m compatible with that in the 1995 Kobe earthquake. Then, the ψ_H value may be estimated at about 460 J/m^3 and the $\overline{\varphi}_H$ value be calculated at 3.68 MJ/m^2 from eq.12 when z_0 is set as 16 km.

6. Scanning ESR microscopy

When we estimate the frictional heat by inversion using eqs.3 and 7 or 9, we need the sequential data of FMR signal along the fault plane. In addition, we must determine the width of heat generation, that is, the thickness of the slip zone on which the frictional heat strongly depends as shown by eq.9. The thickness of the slip zone is considered to be commonly an order of millimeters or less (Sibson, 2003). Therefore, we need the sequential data of FMR signal along the fault plane at a high-resolution of ≤1mm. However it is difficult to measure them using an ordinary ESR spectrometer for grain or powder samples (Fig.2). In this section, I will explain the scanning ESR microscopic technique for sequential high-resolution measurements of FMR signals.

In magnetic resonance, there are two physical quantities for spatially scanning, the external magnetic field and microwaves, however it is technically easier to locally measure ESR signals in the immediate vicinity of the surface of a sample by scanning localized microwave magnetic field leaking out of an aperture of the microwave cavity in a fixed external magnetic field. The scanning of localized microwaves can be carried out by shifting the sample using a mechanical X-Y stage with stepping motors controlled by a computer (Ikeya, 1991). Fig. 21 shows the TE_{111} mode cavity with a pinhole of 2.6 mm φ in diameter (Yamanaka et al., 1992). Ordinary ESR cavities have coils for 100 kHz field modulation inside, however in case of the scanning ESR microscope an external coil for 100 kHz field modulation is set above the pinhole cavity. The sample chip whose surface has been polished using 1 μm-diamond paste is put on the pinhole and the sample arm with the sample is shifted using the mechanical X-Y stage. Since the ESR spectrometer gives a first derivative line, we obtain the ESR absorption curve by integrating the first derivative curve with the magnetic field (Fig. 3). The area of the ESR absorption curve is theoretically proportional to the concentration of unpaired electrons in the sample and magnetic susceptibility. Thus, I set the value obtained by integrating the ESR absorption curve once more as the ESR absorption intensity. The FMR signal intensity is defined as the ESR absorption intensity obtained by integrating the ESR spectrum twice within the range of magnetic field where the FMR signal is detected.

The ESR absorption intensity $I_r(x,t)$ detected by the ESR cavity with a pinhole of radius r at distance x and time t is obtained by integrating the whole absorption intensity within the hemispheric domain V with the volume of $2\pi r^3/3$; the center of the hemisphere is located at distance x.

$$I_r(x,t) = \iiint_V I(x,t)dV = \iiint_V \int_0^t \nu \exp\left[-\frac{E}{RT(x,t)}\right] dtdV \tag{13}$$

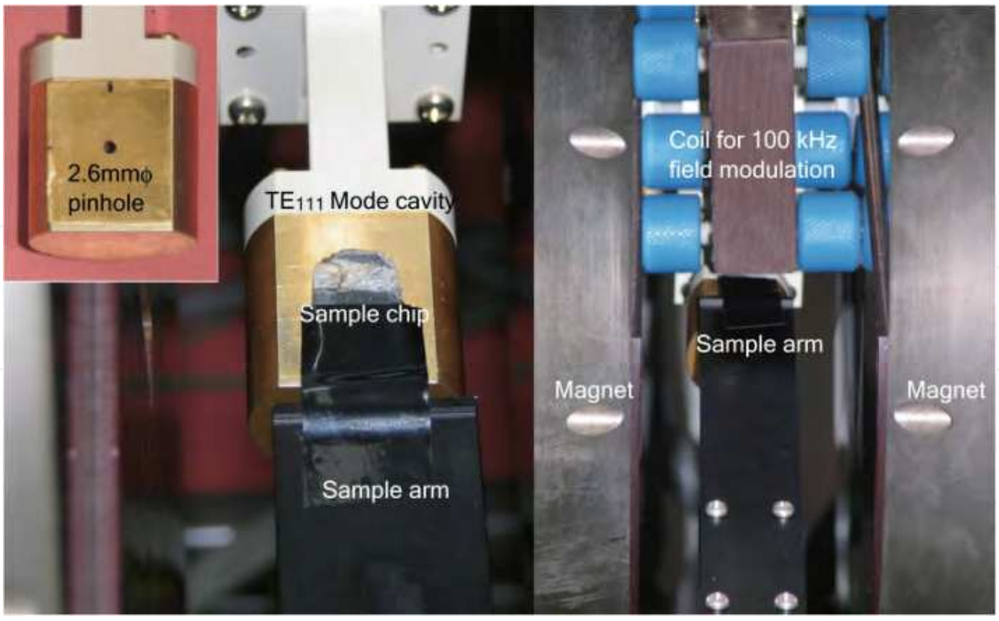

Fig. 21. TE_{111} mode cavity with a pinhole of 2.6 mm φ.

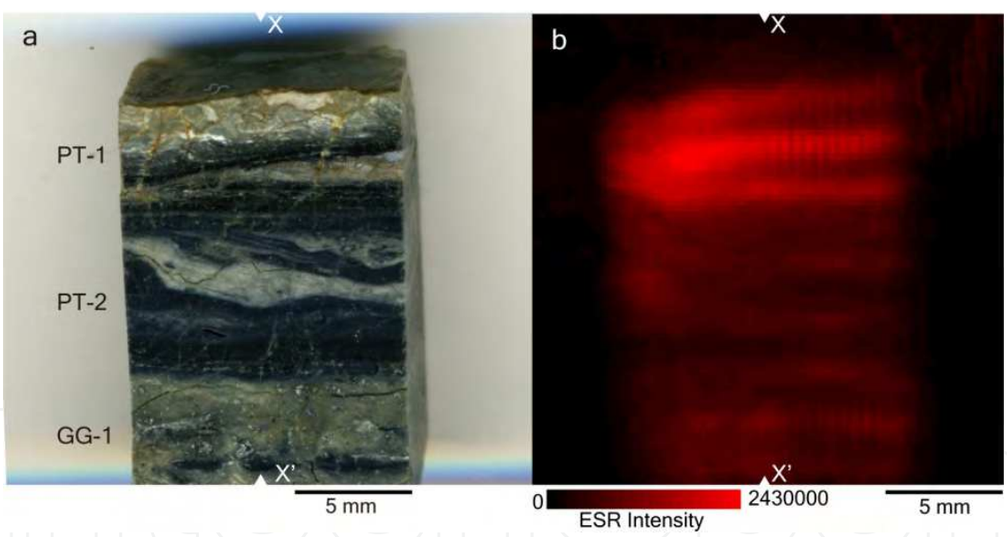

Fig. 22. A 2-D ESR map obtained from the Nojima pseudotachylyte.

Fig. 22 shows a 2-Dimensional ESR map obtained from the sample chip of the Nojima pseudotachylyte. The highest intensity is obtained from the pseudotachylyte vein (PT-1) (Fig. 14). On the other hand, Fig. 23 shows a 1-Dimensional profile obtained from the sample chip along the measuring line X-X'. Measurement conditions are as follows: microwave frequency; 9.388 GHz, microwave power; 100 mW, modulation width; 100 kHz 0.32 mT, scanning speed; 10 s/sweep (2-D) or 2.0 min./sweep (1-D), scan step; 0.25 mm, accumulation; 1 time (2-D) or 3 times (1-D), measurement temperature; room temperature. As shown in Fig. 23, the FMR signals of maghemite are sequentially detected at a resolution of 0.25 mm from the Nojima pseudotachylyte. On the other hand, the detection sensitivity of

the scanning ESR microscope is much lower than the ordinary ESR spectrometer. Since the resolution of the scanning ESR microscope depends on the detection sensitivity, at this stage the limit of resolution is about 0.25 mm.

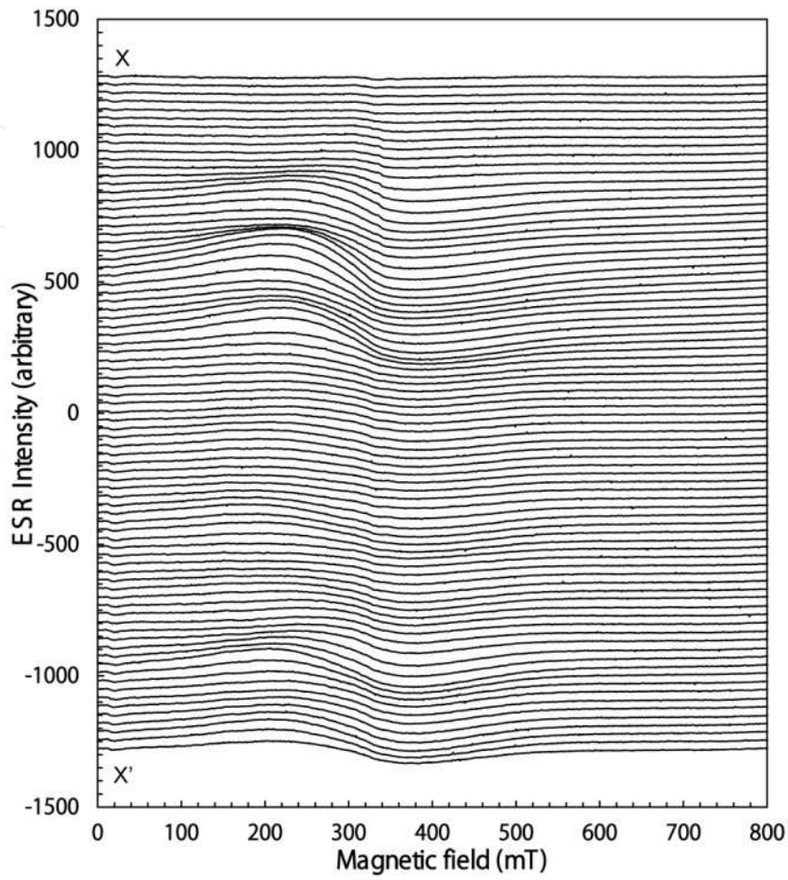

Fig. 23. A 1-D profile obtained from the Nojima pseudotachylyte.

7. Conclusion

I described ESR techniques for detecting seismic frictional heat. We can detect the frictional heat using some FMR signals derived from ferrimagnetic minerals such as maghemite or magnetite produced by heating. To actually estimate the frictional heat from fault rocks, we must carry out high-resolution measurements of FMR signals necessary for determining the width of heat generation. I believe that the scanning ESR microscopic technique makes it possible. Since faults commonly move repeatedly, the frictional heat is also generated repeatedly. Therefore, we need to separate multiplex frictional heating events to accurately estimate the frictional heat energy. Moreover, we need to determine the formation depth of fault rocks used for ESR analyses because the frictional heat commonly increases with increasing the depth of the fault. The frictional heat energy per unit volume is more meaningful than that per unit area. For these purposes, it is important to select fault rock samples with a lot of information revealed by many previous studies, for example the Nojima fault rocks.

8. Acknowledgments

I would like to thank Dr. Wonn Soh and Prof. Sheng-Rong Song for their permission to publish the ESR data on the TCDP Hole B cores in this chapter. This work was funded by Grant-in-Aid for Scientific Research (B) of the Ministry of Education, Science, Sports and Culture, Japan (No.20340139).

9. References

Alger, R. S. (1973). *Electron Spin Resonance: Techniques and Applications,* John Wiley & Sons, Inc., New York.

Butler, R. F. (1992). *Paleomagnetism*, Blackwell Scientific Publications, Boston.

Cardwell, R. K., Chinn, D. S., Moore, G. F., & Turcotte, D. L. (1978). Frictional heating on a fault zone with finite thivkness. *Geophys. J. R. Astron. Soc.,* Vol.52, pp.525−530.

Deer, W. A., Howie, R. A., & Zussman, J. (1992). *An Introduction to the Rock-Forming Minerals* (2nd Edition), Pearson Education Limited, England.

Di Toro, G., Goldsby, D. L., & Tullis, T. E. (2004). Friction falls towards zero in quartz rock as slip velocity approaches seismic rates. *Nature,* Vol.427, pp.436–439.

Fabbri, O., Lin, A., & Tokushige, H. (2000). Coeval formation of cataclasite and pseudotachylyte in a Miocene forearc granodiorite, southern Kyushu, Japan. *J. Struct. Geol.,* Vol.22, pp.1015–1025.

Ferré, E. C., Zechmeister, M. S. , Geissman, J. W., MathanaSekaran, N., & Kocak, K. (2005). The origin of high magnetic remanence in fault pseuodtahcylites: Theoretical considerations and implication for coseismic electrical currents. *Tectonophys.*, Vol.402, pp.125–139.

Fukuchi, T. (1989) Theoretical study on frictional heat by faulting using electron spin resonance. *Appl. Radiat. Isot.*, Vol.40, pp.1181–1193.

Fukuchi, T. (1992). ESR studies for absolute dating of fault movements. *J. Geol. Soc. London*, Vol.149, pp.265–272.

Fukuchi, T., & Imai, N. (2001). ESR and ICP analyses of the DPRI 500m drilling core samples penetrating through the Nojima fault, Japan. *Island Arc*, Vol.10, pp.465–478.

Fukuchi, T. (2003). Strong ferrimagnetic resonance signal and magnetic susceptibility of the Nojima pseudotachylyte in Japan and their implication for coseismic electromagnetic changes. *J. Geophys. Res.*, Vol.108, No.B6, 2312, doi:10.1029/2002JB002007.

Fukuchi, T., Mizoguchi, K., & Shimamoto, T. (2005). Ferrimagnetic resonance signal produced by frictional heating: A new indicator of paleoseismicity. *J. Geophys. Res.*, Vol.110, B12404, doi:10.1029/2004JB003485.

Fukuchi, T., Yurugi, J., &Imai, N. (2007). ESR detection of seismic frictional heating events in the Nojima fault drill core samples, Japan. *Tectonophys.*, Vol.443, pp.127–138.

Han, R., Shimamoto, T., Ando, J., & Ree, H.-H. (2007). Seismic slip record in carbonate-bearing fault zones: An insight from high-velocity friction experiments on siderite gouge. *Geology*, Vol.35, pp.1131–1135.

Hirono, T., Ikehara, M., Otsuki, K., Mishima, T., Sakaguchi, M., Soh, W., Omori, M., Lin, W., Yeh, E.-C., Tanikawa, W., Wang, C.-Y. (2006). Evidence of frictional melting from disk-shaped black material, discovered within the Taiwan Chelungpu fault system. *Geophys. Res. Lett.,* Vol.33, L19311, doi:10.1029/2006GL027329.

Ikeya, M. (1991). Electron spin resonance (ESR) microscopy in materials science. *Annu. Rev. Mater. Sci.*, Vol.21, pp.45–63.

Ikeya, M. (1993). *New Applications of Electron Spin Resonance, Dating, Dosimetry and Microscopy,* World Scientific, Singapore.

Kanamori, H., Anderson, D. L., & Heaton, T. H. (1998). Frictional melting during the rupture of the 1994 Bolivian earthquake. *Science*, Vol.279, pp.839–842.

Kanamori, H., & Heaton, T. H. (2000). Microscopic and macroscopic physics of earthquakes, in *GeoComplexity and the Physics of Earthquakes*, *Geophys. Monogr. Ser.*,vol.120, edited by J. B. Rundle, D. L. Turcotte, and W. Klein, pp. 147–163, AGU, Washington, D. C.

Kittel, C. (2005). *Introduction to Solid State Physics* (8th Edition), John Wiley & Sons, Inc., New York.

Lachenbruch, A. H., & Sass, J. H. (1980). Heat flow and energetic of the San Andreas fault zones. *J. Geophys. Res.* , Vol.85, pp.6249−6272.

Lachenbruch, A. H., & Sass, J. H. (1992). Heat flow from Cajon Pass, fault strength and tectonic implications. *J. Geophys. Res.* , Vol.97, pp.4995−5015.

Ma, K.-F., Tanaka, H., Song, S.-R., Wang, C.-Y., Hung, J.-H., Tsai, Y.-B., Mori, J., Song, Y.-F., Yeh, E.-C., Soh, W., Sone, H., Kuo, L.-W., Wu, H.-Y. (2006). Slip zone and energetic of a large earthquake from the Taiwan Chelungpu-fault Drilling Project. *Nature,* Vol.444, pp.473−476, doi:10.1038/nature05253.

McKenzie, D., & Brune, J. N. (1972). Melting on fault planes during large earthquakes. *Geophys. J. R. Astron. Soc.,* Vol.29, pp.65−78.

Murata, A., Takemura, K., Miyata, T., & Lin, A. (2001). Quaternary vertical offset and average slip rate of the Nojima fault on Awaji Island, Japan. *Island Arc,* Vol.10, Issue 3/4, pp.360−367.

Otsuki, K., Monzawa, N. & Nagase, T. (2003). Fluidization and melting of fault gouge during seismic slip: Identification in the Nojima fault zone and implications for focal earthquake mechanisms. *J. Geophys. Res.,* Vol.108, No.B6, 2192, doi:10.1029/2001JB001711.

Sibson, R. H. (2003). Thickness of the seismic slip zone. *Bull. Seismol. Soc. Am.*, Vol.93, pp.1169–1178.

Smit, J., & Wijn, H. P. J. (1965). *Ferrites, Physical Properties of Ferrimagnetic Oxides in Relation to Their Technical Applications* (International Edition), Tokyo Electrical Engineering College Press, Tokyo.

Yamanaka, C., Ikeya, M. & Hara, H. (1992). ESR cavities for In Vivo dosimetry of tooth enamel. *Appl. Radiat. Isot.*, Vol. 44,pp. 77–80.

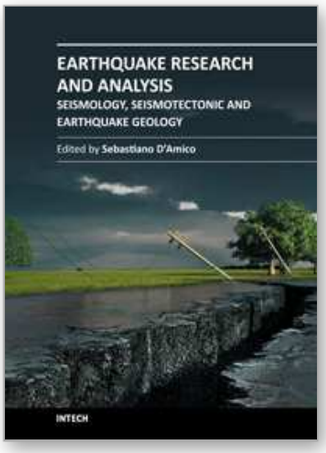

Earthquake Research and Analysis - Seismology, Seismotectonic and Earthquake Geology

Edited by Dr Sebastiano D'Amico

ISBN 978-953-307-991-2
Hard cover, 370 pages
Publisher InTech
Published online 08, February, 2012
Published in print edition February, 2012

This book is devoted to different aspects of earthquake research. Depending on their magnitude and the placement of the hypocenter, earthquakes have the potential to be very destructive. Given that they can cause significant losses and deaths, it is really important to understand the process and the physics of this phenomenon. This book does not focus on a unique problem in earthquake processes, but spans studies on historical earthquakes and seismology in different tectonic environments, to more applied studies on earthquake geology.

How to reference

In order to correctly reference this scholarly work, feel free to copy and paste the following:

Tatsuro Fukuchi (2012). ESR Techniques for the Detection of Seismic Frictional Heat, Earthquake Research and Analysis - Seismology, Seismotectonic and Earthquake Geology, Dr Sebastiano D'Amico (Ed.), ISBN: 978-953-307-991-2, InTech, Available from: http://www.intechopen.com/books/earthquake-research-and-analysis-seismology-seismotectonic-and-earthquake-geology/esr-techniques-for-the-detection-of-seismic-frictional-heat

INTECH
open science | open minds

InTech Europe
University Campus STeP Ri
Slavka Krautzeka 83/A
51000 Rijeka, Croatia
Phone: +385 (51) 770 447
Fax: +385 (51) 686 166
www.intechopen.com

InTech China
Unit 405, Office Block, Hotel Equatorial Shanghai
No.65, Yan An Road (West), Shanghai, 200040, China
中国上海市延安西路65号上海国际贵都大饭店办公楼405单元
Phone: +86-21-62489820
Fax: +86-21-62489821

© 2012 The Author(s). Licensee IntechOpen. This is an open access article distributed under the terms of the Creative Commons Attribution 3.0 License, which permits unrestricted use, distribution, and reproduction in any medium, provided the original work is properly cited.